







## RESEARCH ARTICLE

10.1029/2022JA030575

# Magnetic Fields and Plasma Motions in a Hybrid Martian Magnetosphere

E. Dubinin<sup>1</sup> , M. Fraenz<sup>1</sup> , M. Pätzold<sup>2</sup>, S. Tellmann<sup>2</sup>, R. Modolo<sup>3</sup> , G. DiBraccio<sup>4</sup> , J. McFadden<sup>5</sup>, and J. Espley<sup>4</sup>

<sup>1</sup>Max-Planck-Institute for Solar System Research, Göttingen, Germany, <sup>2</sup>Rheinisches Institut fuer Umweltforschung, Abteilung Planetenforschung, Cologne, Germany, <sup>3</sup>LATMOS/IPSL, UVSQ Universite, Paris-Saclay, UPMC University Paris CNRS, Guyancourt, France, <sup>4</sup>NASA Goddard Space Flight Center, Greenbelt, MD, USA, <sup>5</sup>Space Sciences Laboratory, U.C. Berkeley, Berkeley, CA, USA

### Key Points:

- The Martian magnetosphere contains elements of induced and intrinsic origin
- Dynamics of ion fluxes in the magnetic tail, is mainly controlled by induced features
- Reconnection of the interplanetary magnetic field with low-order harmonics of the crustal field leads to twisting of the tail and formation of hybrid magnetosphere

### Correspondence to:

E. Dubinin,  
dubinin@mps.mpg.de

### Citation:

Dubinin, E., Fraenz, M., Pätzold, M., Tellmann, S., Modolo, R., DiBraccio, G., et al. (2023). Magnetic fields and plasma motions in a hybrid Martian magnetosphere. *Journal of Geophysical Research: Space Physics*, 128, e2022JA030575. <https://doi.org/10.1029/2022JA030575>

Received 25 APR 2022  
Accepted 16 DEC 2022

**Abstract** The Martian magnetosphere contains elements of induced and intrinsic origin. To display them one must use different coordinate systems. Although the solar-electric coordinate system (Mars Solar Electric [MSE]) adequately describes the main features of the induced magnetosphere, it removes/suppresses aspects caused by the crustal magnetic sources while rotating the spacecraft position to the MSE-coordinate system and averaging over many orbits. On the other hand, to observe effects of the crustal field one should use the solar orbital coordinates (Mars Solar Orbital [MSO]). To find a compromise and keeping in mind that the most probable value of the clock angle of the interplanetary magnetic field (IMF) on the Mars orbit is  $\sim 90^\circ$  we can consider separately cases with positive and negative  $B_y$  components of the IMF. It is shown that dynamics of ion fluxes in the distant regions of the magnetosphere is mainly controlled by induced features. However, reconnection of the draping IMF with crustal field leads to a twisting of the classical draping configuration. Despite of the very intricate local geometry of the crustal field, the low-order harmonics of the magnetic field and mainly the dipole component determine the reconnection sites, at least, statistically for many Mars rotations. For different signs of the  $B_y$  component of the IMF these sites occur either in the +Y-MSO or –Y-MSO hemispheres. As a result, statistically the magnetosphere of Mars looks like a hybrid magnetosphere formed during the solar wind interaction with the obstacle which simultaneously contains an extended ionosphere and a weak dipole magnetic field.

## 1. Introduction

The absence of a global magnetic field at Mars leads to a nearly direct interaction of the solar wind with the ionosphere and to the formation of an induced magnetosphere where the interplanetary magnetic field (IMF) drapes around the ionospheric obstacle. However, the existence of strong localized crustal magnetic fields (Acuña et al., 1999; Connerney et al., 2005) adds features typical for planets with a global intrinsic magnetic field. As a result, the Martian magnetosphere contains elements of induced and intrinsic origin (see e.g., Dubinin, Luhmann, & Slavin, 2020; Halekas et al., 2021; Nagy et al., 2004). To display these components one must use different coordinate systems. Effects of the induced origin are well observed utilizing the Mars Solar Electric (MSE) coordinate system which has the  $X_{MSE}$  axis antiparallel to the upstream solar wind flow, the  $Y_{MSE}$  axis along the cross-flow magnetic field component of the IMF in the solar wind, and the  $Z_{MSE}$  axis pointing in the direction of the solar wind motional electric field ( $-V_{sw} \times B_{IMF}$ ), where  $V_{sw}$  and  $B_{IMF}$  are the vectors of the velocity and the magnetic field in the solar wind, respectively (Dubinin et al., 1996; Moore et al., 1990; Russell et al., 1995; Yeroshenko et al., 1990). Analysis of data of the MAVEN mission in MSE coordinates allowed to find out many important induced features related to the direction of the motional electric field in the solar wind, for example, an asymmetry in the escape ion fluxes with an ion plume at the dayside (Dong et al., 2015; Dubinin et al., 2011), an ion trail at the nightside (Dubinin et al., 2018), ion extraction from the ionosphere (Dubinin et al., 2021) and an asymmetry of magnetic field draping (Chai et al., 2019; Dubinin et al., 2018, 2021; Ramstad et al., 2020). Although the MSE coordinate system adequately describes the main features of the induced magnetosphere of Mars, it removes/suppresses aspects caused by the crustal magnetic sources while rotating the spacecraft position vector to the MSE-coordinate system and averaging over many orbits (see e.g., Dubinin et al., 2021).

The influence of the crustal field is rather complicated because of the intricate, localized topology of the crustal field lines coupled with the Martian rotation. Analysis of the Mars Global Surveyor (MGS) measurements at

© 2022 The Authors.

This is an open access article under the terms of the [Creative Commons Attribution-NonCommercial License](https://creativecommons.org/licenses/by-nc/4.0/), which permits use, distribution and reproduction in any medium, provided the original work is properly cited and is not used for commercial purposes.

400 km performed by Brain et al. (2006) have found significant deviations from the ideal draping geometry. The magnetic field topology traced by a study of the electron dynamics (Xu et al., 2019) contains different classes of the field lines. Within the draping IMF, closed loops of the field lines connected to the crustal field sources, open field lines with one end in the solar wind and another end on the Mars surface, formed by the reconnection between the crustal field and the IMF—are present (Weber et al., 2017, 2019; Xu et al., 2017, 2020). As a result, the magnetic field topology within the tail varies with solar wind pressure (Weber et al., 2019, 2020) and the IMF direction (Xu et al., 2020). Precipitation of electrons along the open field lines produce discrete aurora typical for the Earth magnetosphere (Girazian et al., 2021; Lillis et al., 2018; Schneider et al., 2021). It is worth noting that crustal magnetic fields on Mars not only change the field topology but also significantly vary the density distribution in the upper ionosphere (Andrews et al., 2013; Dubinin et al., 2012, 2016) and influence the ion loss (Dubinin, Fraenz, et al., 2020; Fan et al., 2019, 2020; Fang et al., 2015, 2017; Weber et al., 2021).

Nevertheless, one can observe a global effect of the crustal fields while considering a statistical field configuration by averaging over many Mars rotations and using the Mars Solar Orbital (MSO) coordinates in which the  $X$ -axis is directed from the center of Mars to the Sun, the  $Z$ -axis is perpendicular to the planetary orbital plane and directed to the north, and  $Y$  completes the right-handed system. Since the most probable value of the clock angle of the IMF on the Mars orbit is  $\sim 90^\circ$  (DiBraccio et al., 2018; Liu et al., 2021), that is, the IMF is mostly within the orbital plane, it is reasonable to consider separately cases with positive and negative  $B_y$  components of the IMF. The net result is the appearance of a twisted magnetotail either in the clockwise or anticlockwise direction depending on sign of the  $B_y$  component in the solar wind (DiBraccio et al., 2018, 2022; Dubinin et al., 2017) that resembles topology of a hybrid magnetosphere with elements of the induced and intrinsic magnetospheres (Dubinin et al., 1980). According to DiBraccio et al., 2022 a twisting can reach  $\sim 60^\circ$  away from its expected location based on IMF draping. DiBraccio et al. (2022) have shown that this effect is a robust feature and is displayed for different conditions with only a variation in the twist value.

Such an approach with utilization of the MSO coordinate system for two classes of the IMF ( $\pm B_y$ ) allows to study the induced and intrinsic aspects of the Martian magnetosphere at the same time. It is worth mentioning that such approach ideally presupposes the existence of an upstream monitor at Mars which provides the IMF while the inner magnetosphere is explored, that is unfortunately not the case for Mars. Therefore we utilize the magnetic field measurements made by MAVEN on the same orbits when the spacecraft was in solar wind or sometimes even in the magnetosheath. Given the continuous variations in the upstream conditions this method can lead to some errors although, because of a large statistics, this approach seems to be a reasonable approximation.

In this investigation we focus on characterizing the main phenomenological features of the hybrid Martian magnetosphere, including the topology of the magnetic field as well as the induced ionospheric dynamics.

## 2. Instrumentation

The Mars Atmosphere and Volatile Evolution (MAVEN) spacecraft arrived at Mars in September 2014 to study the processes in the upper atmosphere/ionosphere and its interaction with the solar wind (Jakosky et al., 2015). MAVEN was inserted into an elliptical orbit with periapsis and apoapsis of 150 and 6,200 km, respectively, and with a period of 4.5 hr. Unique capabilities of MAVEN measurements allow us to investigate the macroscopic flows, fields and forces in the Martian space (Halekas et al., 2017). In this paper, we discuss observations made by the magnetometer (MAG) and the Supra-Thermal And Thermal Ion Composition (STATIC) instrument from November 2014 to May 2018. MAVEN's MAG (Connerney et al., 2015) samples the magnetic environment at Mars with a maximum rate of 32 vectors/s. We use values of the magnetic field vector sampled at 4s resolution to infer the local magnetic field orientation. We derive the IMF orientation by taking the median value of the magnetic field vector components from 30 min around the time where the maximum proton velocity measured by the solar wind monitor SWIA (Halekas et al., 2015) was observed. We do not exclude orbits with a high variation of the field vector. We processed all orbits in order to study the global features without any assumptions about stationarity of the IMF orientation. During the orbits when MAVEN was not in the solar wind we use the magnetic field measurements in the magnetosheath. Note that for these cases the clock angle errors due to the IMF deformations may appear (Dong et al., 2019). The STATIC instrument measures energy spectra of ion fluxes in the range of 0.1 eV–30 keV and the ion composition (McFadden et al., 2015). The STATIC instrument samples all received time-of-flight events onboard with 64 energy bins, 64 mass bins,  $16 \times 16$  field of view bins at 4s time resolution. Because the resulting matrix is far too big to be downloaded as a whole, only down-sampled

“products” are transmitted which represent sums over one or more dimensions of the original 5-dimensional matrix (McFadden et al., 2015). Not all products are transmitted at the same time. We take a subset of these products (c0,cf,d1,ce,d0,cd,cc,ca—depending on availability) to reconstruct a matrix  $M$  with the dimension of 32 energy bins, 4 mass bins,  $16 \times 4$  field of view bins at 4s time resolution by linear interpolation from this subset. In each interpolation step we normalize the respective dimension to guarantee that the sums over all dimensions of  $M$  stays the same as for the original products. By this procedure we get a time series with commensurate sampling in energy, field of view, and time for the 4 major ion groups ( $H^+$ ,  $He^{++}$ ,  $O^+$ ,  $O_2^+$ ). From this time series we calculate density, velocity, and temperature for these groups with even time sampling. We made also corrections using the values of the s/c potential presented by the STATIC team (Lavraud & Larson, 2016).

### 3. Observations

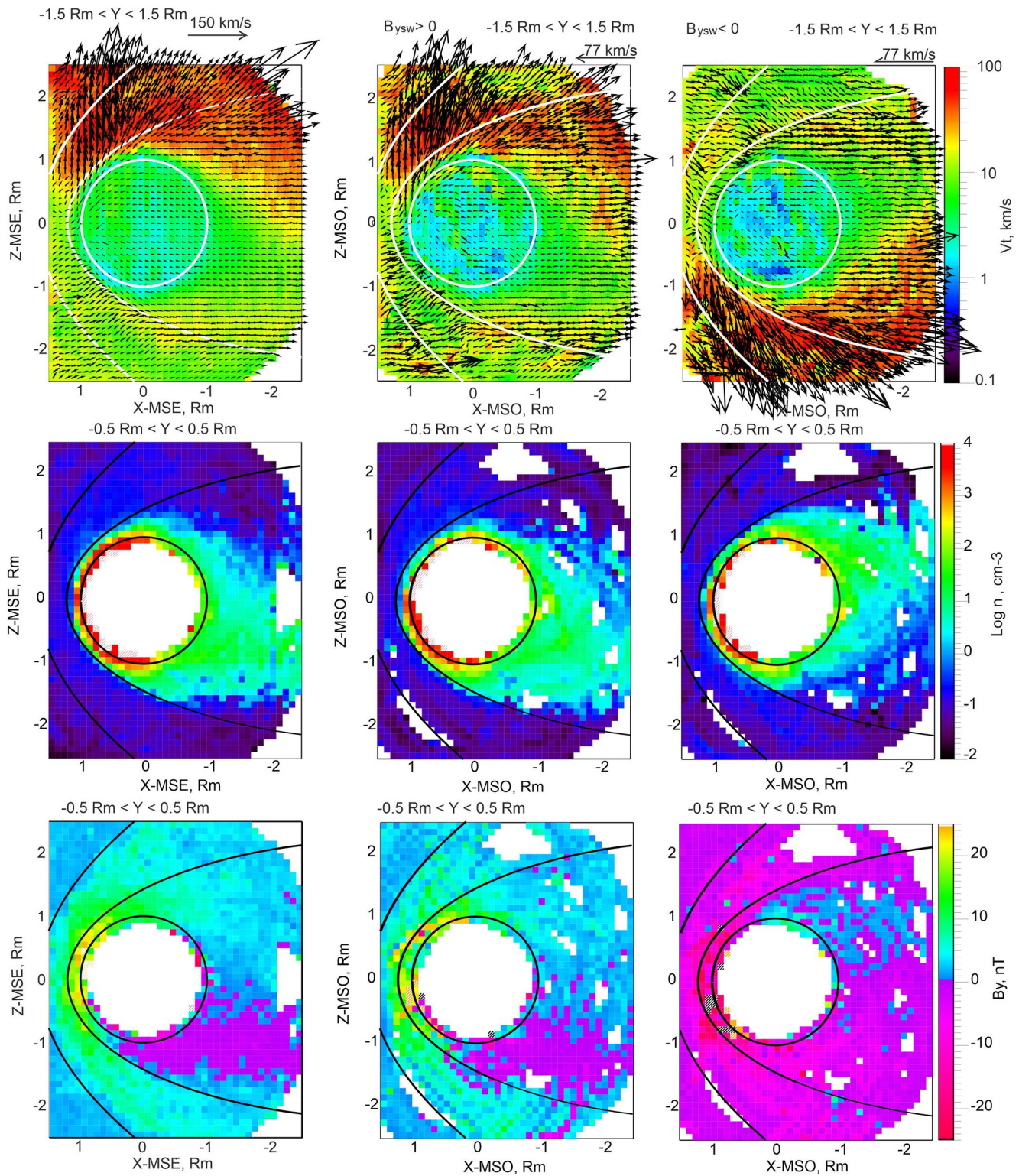
#### 3.1. Outer Part of the Martian Magnetosphere and Tail

Figure 1 compares maps of the different values in the MSE (left column) and the MSO coordinates for  $B_{y_{sw}} > 0$  (middle column), and for  $B_{y_{sw}} < 0$  (right column). The size of each spatial bin is  $0.1 R_M$ . The data are shown for XZ-planes. White and black curves present the positions of Mars, and the statistical mean locations of magnetospheric boundary (MB) and the bow shock (BS). We used the curves by Vignes et al. (2000) for BS and modified curves of Vignes et al. (2000) for the MB location, for better agreement with ASPERA-3 observations in the noon sector (Dubinin et al., 2006). It is worth noting that the average locations of these boundaries vary under the influence of different drivers (e.g., Garnier et al., 2002), including also the season and the solar cycle with slightly different parameters for the conics for the different Martian years covered by MAVEN (Simon Wedlund et al., 2022 and references therein).

The top row presents the total bulk velocity of oxygen ions  $V = (n_{O_2^+} V_{O_2^+} + n_{O^+} V_{O^+}) / (n_{O_2^+} + n_{O^+})$  ( $-1.5R_M \leq Y \leq 1.5R_M$ ). Arrows show the projection of the bulk velocity vector onto the XZ planes. It is observed that a velocity pattern in the outer part of the Martian magnetosphere is controlled by the sign of  $B_{y_{sw}}$  (or by Z-component of  $\vec{E} = -\vec{V}_{sw} \times \vec{B}_{sw}$ ) with a reversal of the ion plume position toward the southern hemisphere for  $B_{y_{sw}} < 0$ . In MSE coordinates the picture is similar to the one for  $B_{y_{sw}} > 0$ . The second row depicts maps of the oxygen number density ( $n_{O_2^+} + n_{O^+}$ ) ( $-0.5R_M \leq Y \leq 0.5R_M$ ). The position of the ion trail of dense plasma in the tail, which is shifted to the opposite hemisphere as compared to the ion plume, is vertically flipping with a change of sign of the  $B_{y_{sw}}$  component. Comparing maps of the velocity and density we observe that ion velocities in the ion trail are small. In MSE coordinates the density distribution in the tail is similar to the one for  $B_{y_{sw}} > 0$ . The bottom row presents the value of the local  $B_y$  component of the magnetic field ( $-0.5R_M \leq Y \leq 0.5R_M$ ). The area of the sign reversal of the  $B_y$  component corresponding to a wrapping of the field lines around Mars, generally coincides with the position of the ion trail and is also controlled by the sign of the  $B_{y_{sw}}$  component in the solar wind. A reversal of the sign of  $B_y$  in the tail must result in appearance of the magnetic tension forces which operate in the sunward direction. Such forces can decelerate the outflowing plasma and increase their density. A reversal of the sign of the  $B_y$  component is better seen in the MSE coordinates indicating the induced origin of such a change of the magnetic topology.

Figure 2 shows maps of different parameters in a cut through the Martian tail in the plane YZ-MSO at  $-3R_M \leq X \leq -1.3 R_M$  for positive and negative  $B_{y_{sw}}$ . Panels (a) and (a1) present the total number density of oxygen ions ( $n_{O^+} + n_{O_2^+}$ ). A clear shift of the density distribution in the direction opposite to the direction of the motional electric field in the solar wind provide evidence that the induced features controlled by the sign of the  $B_{y_{sw}}$  component dominate in the tail. On the other hand, there are also some signatures of the influence of the crustal magnetic field. The number density at  $Z > 1R_M$  at  $B_{y_{sw}} > 0$  is significantly less than at  $Z < -1R_M$  at  $B_{y_{sw}} < 0$ . It is in agreement with the observations of a thicker ionosphere above the regions with crustal magnetic fields (Andrews et al., 2013; Dubinin et al., 2012, 2016). Panels (b) and (b1) depict the number density of the protons with  $E > 30$  eV which might be reasonably attributed to the solar wind population. Panels (c) and (c1) compare the bulk velocities of oxygen ions. It is observed an asymmetry in the oxygen ions distribution of accelerated by the motional electric field oxygen ions in both hemispheres. Panels (d) and (d1) present the fluxes of oxygen ions with  $E > 30$  eV. Such fluxes allow monitoring of the current sheet in the tail (Dubinin et al., 2017). We observe a twisting of the current sheet in accordance with a twisting of the tail lobes (DiBraccio et al., 2018, 2022). Such a





**Figure 1.** Left column, from top to bottom: Maps in the XZ-Mars Solar Electric plane of the velocity vectors of oxygen ions imposed on color plot of the total oxygen ion velocity  $V_i$  (bin size is  $0.1 R_M$ ), density of oxygen ions,  $B_y$  component of the magnetic field. The middle and right columns present the same parameters plotted in Mars Solar Orbital coordinates for different signs of the  $B_y$  component in the solar wind, respectively. In red and black shaded bins the values are higher (lower) than the upper (lower) values in the color bars, respectively. Statistically mean positions of the bow shock (Vignes et al., 2000) and the magnetospheric boundary (Dubinin et al., 2006) are also shown.



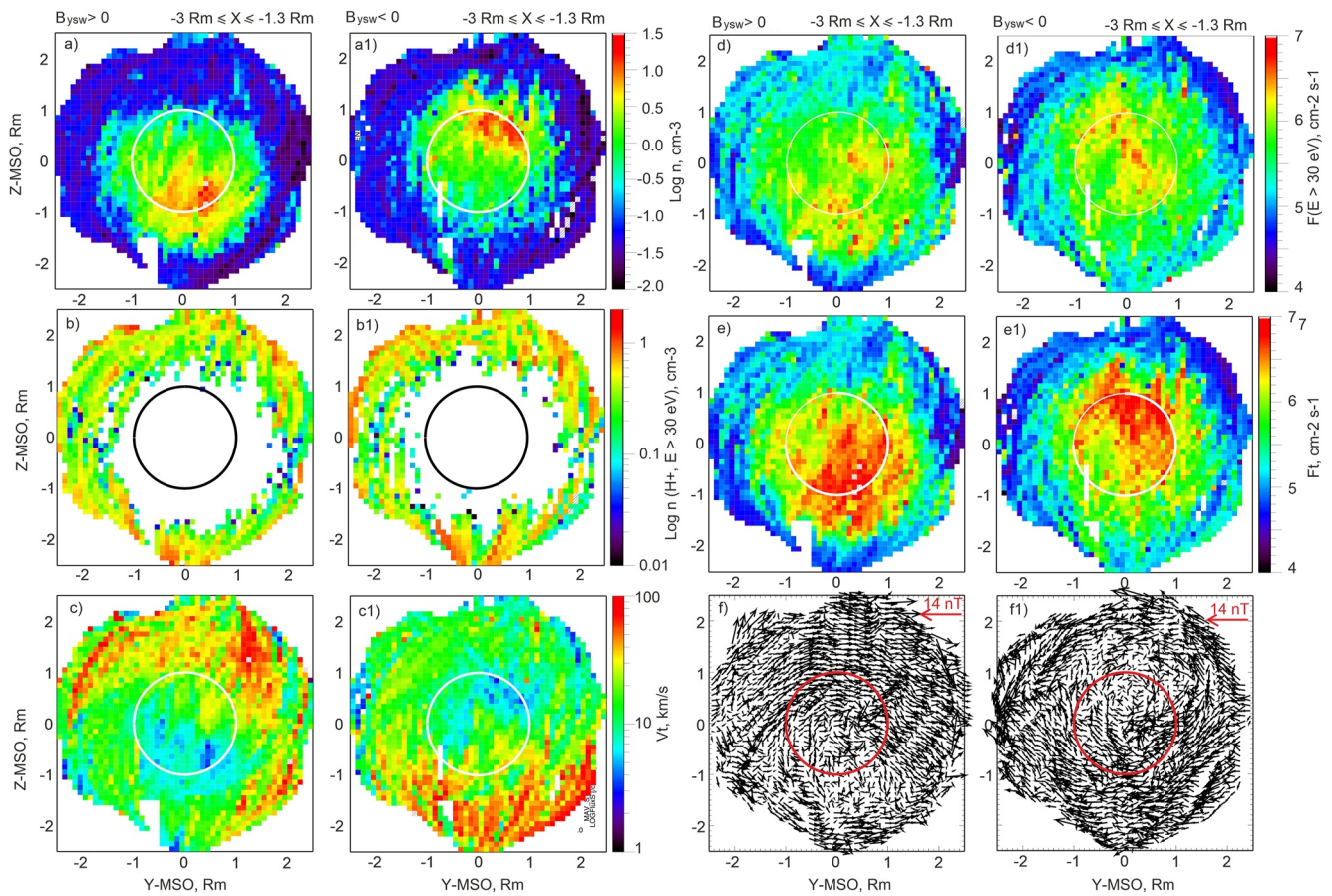


**Figure 2.** Maps of different parameters in the YZ-Mars Solar Orbital plane in the tail ( $-3R_M \leq X \leq -1.3R_M$ ) for  $B_{ysw} > 0$  and  $B_{ysw} < 0$ . Panels (a) and (a1): density of oxygen ions; (b) and (b1): density of the solar wind protons; (c) and (c1): total velocity of oxygen ions; (d) and (d1): fluxes of oxygen ions with  $E > 30$  eV; (e) and (e1): total fluxes of oxygen ions; (f) and (f1):  $B_{yz}$  projections of the magnetic field.

twisting is an obvious indicator of the hybrid character of the Martian magnetosphere. A twisting of lobes is also well seen while plotting the total fluxes of oxygen ions in the tail (panels (e) and (e1)). A shift of fluxes toward the dusk sector is another interesting feature. Panels (f) and (f1) compare maps of the magnetic field projections onto the YZ-MSO planes. We observe a draping of the magnetic field along the  $\pm Z$  axis determined by the sign of the  $B_{ysw}$  component that is in accordance with presentations of the data in MSE-coordinates (Chai et al., 2019; Dubinin et al., 2018; Ramstad et al., 2020).

The twisting of the tail lobes also results in a difference in their size between the northern and southern hemispheres. Figure 3 shows maps of the  $B_x$  component within the nominal position of the magnetosphere boundary in the XY-MSO planes for  $Z > 0$  (upper row) and  $Z < 0$  (lower row). Color depicts the value of the  $B_x$  component, where different signs correspond to different lobes. We observe that in the northern hemisphere for  $B_{ysw} > 0$  (left column) the lobe at  $Y < 0$  is expanding toward the  $+Y$  areas, while in the southern hemisphere, the lobe at  $Y > 0$  expands toward the  $-Y$  regions. The reversed picture is seen in the case of  $B_{ysw} < 0$  (right column). This may happen due to reconnection processes which add or reduce the magnetic field flux in the different areas similar as it happens at the Earth.

### 3.2. Inner Part of the Martian Magnetosphere

Figure 4 (panels (b) and (b1)) shows maps of the unit vectors of the magnetic field in the YZ-MSO planes at the dayside ( $X > 0$ ) for  $B_{ysw} > 0$  and  $B_{ysw} < 0$ , respectively. We only utilize the data within the magnetosphere boundary at altitudes below 1,000 km. To compare changes of the data presented in the MSO-coordinates panels (a) and (a1) show the unit vectors in the MSE-coordinates. Solid red lines show the projection of the field lines based on

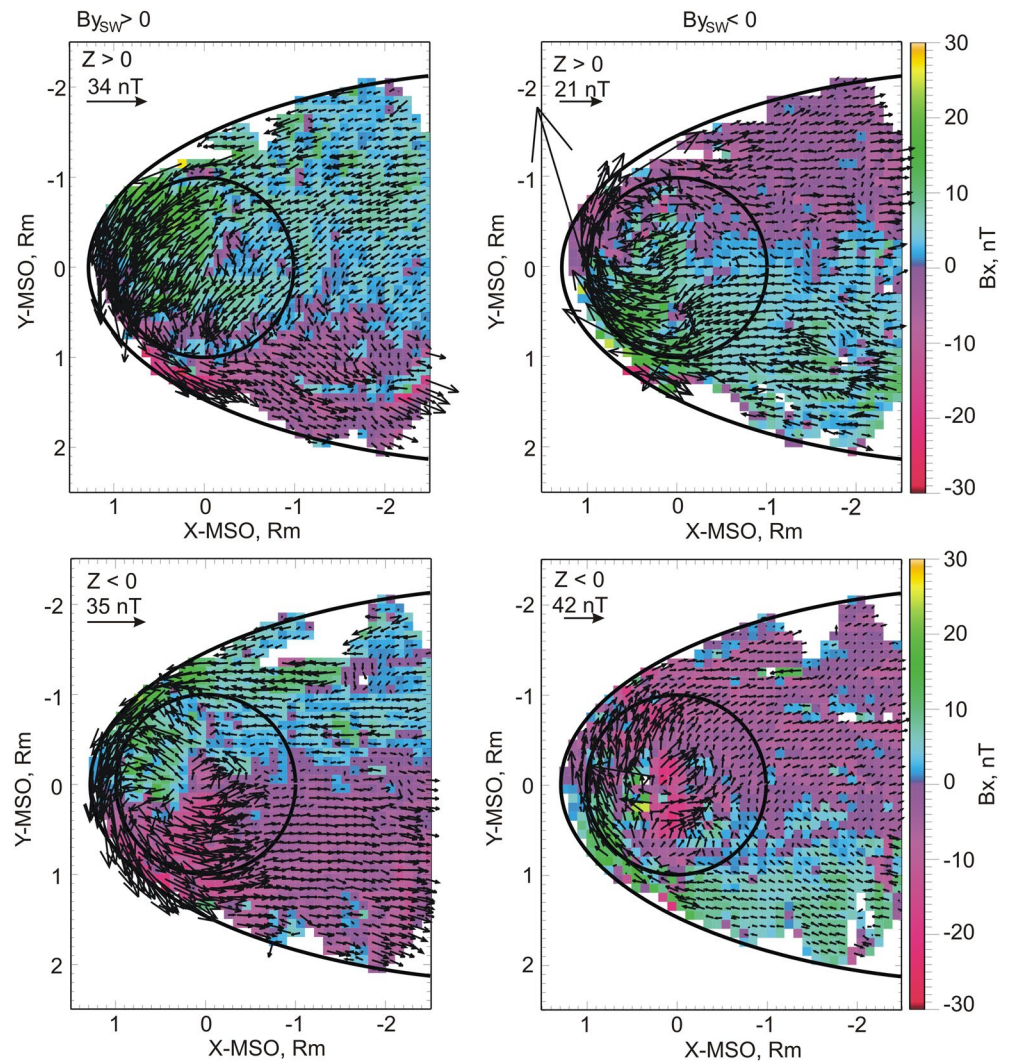


**Figure 3.** Left column: Maps of the magnetic field vectors onto XY-Mars Solar Orbital planes in the northern and southern hemispheres for  $B_{y_{sw}} > 0$ . Color depict the  $B_x$  value; Right column: the same for  $B_{y_{sw}} < 0$ . Statistically mean position of the magnetospheric boundary (Dubinin et al., 2006; Vignes et al., 2000) is also shown.

the unit vectors. It is worth noting that panel (a1) is constructed by the vertical and horizontal flipping of panel (a). In the upper hemisphere, in MSE coordinates (panel (a)), we observe a reversal of the draping geometry just where the formation of the plasma sheet begins. A clear asymmetry between the upper ( $E^+$ ) and the lower ( $E^-$ ) hemispheres is also evident. Such a picture was already discussed in (Dubinin et al., 2021). In MSO-coordinates for  $B_{y_{sw}} > 0$  we see a clear clockwise skewness of the field lines in the northern hemisphere (panel (b)) as compared to picture in MSE-coordinates (panel (a)). Such a twist is also seen on panel (c) which present the  $B_x$  component of the magnetic field. A strong skewness of the transverse component  $B_{yz}$  of the magnetic field indicates that reconnection occurs in the dusk sector ( $Y-MSO > 0$ ). Then, pieces of the field lines at the dawn sector ( $Y-MSO < 0$ ) are slipping around Mars in the  $+Z$ -direction faster than the pieces at the duskside and a skewness appears.

In the southern hemisphere (panel (b)), the field topology is characterized by a strong  $B_z$  component in the  $-Y$  sector. The same features are revealed if we only consider the altitude interval of 300–500 km (panel (d)). For  $B_{y_{sw}} < 0$ , in the northern hemisphere, a picture is rather irregular while in the southern hemisphere we observe a clear twisting in anticlockwise direction (panel (c1)).

The skewness of the magnetic field lines and their differential transport around Mars caused by the reconnection occurred either in the  $+Y$  or  $-Y$  hemisphere must lead to unforeseen reversal of the  $B_x$  component. Figure 5 shows, for example, the unit vectors of the projections of the magnetic field onto the XZ-MSO planes at different



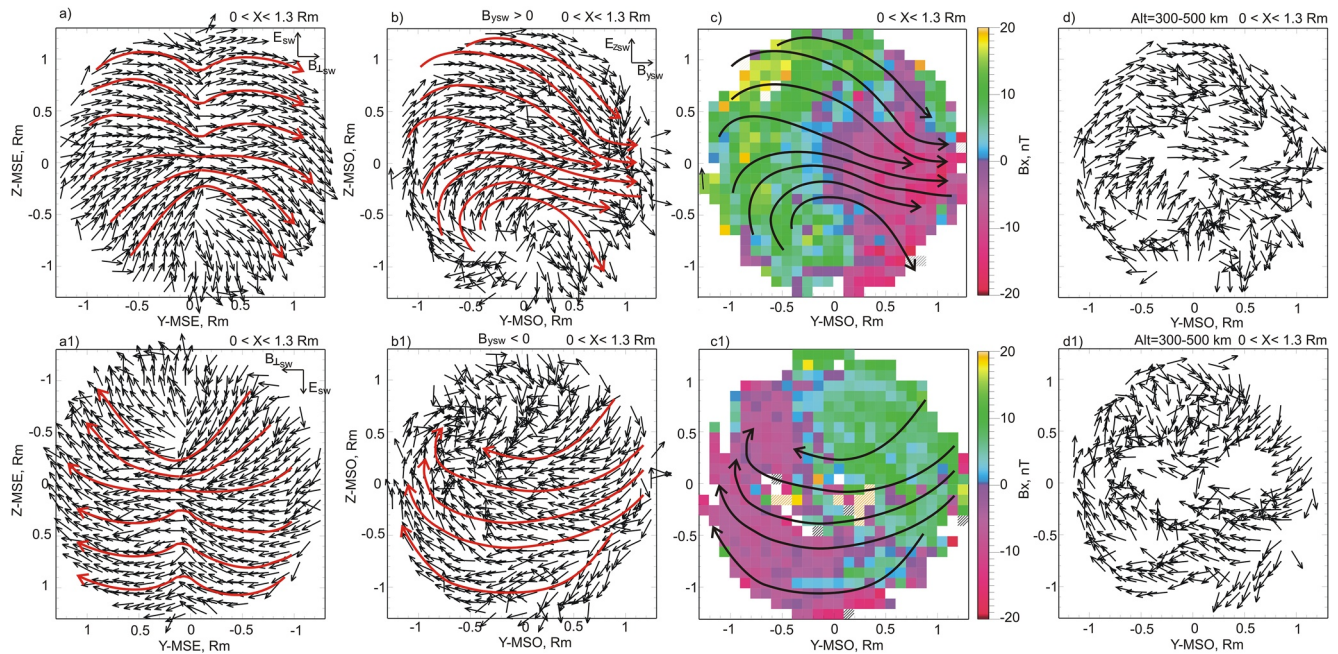


**Figure 4.** Panel (a): Projections of the unit vectors of the magnetic field onto the YZ-Mars Solar Electric plane within the Martian magnetosphere at the dayside for altitudes less 1,000 km. Red curves show projections of the field lines; (b): similar plot in Mars Solar Orbital coordinates for  $B_{y_{sw}} > 0$ ; (c): map of the  $B_x$  component of the magnetic field for  $B_{y_{sw}} > 0$ ; black curves are projections of the field lines; (d) projections of the unit vectors of the field at altitudes between 300 and 500 km. Panel (a1) is a vertical and horizontal mirror of panel (a); panels (b1), (c1) and (d1) show the same values as in panels (b), (c), (d) but for  $B_{y_{sw}} < 0$ .

+Y-MSO positions for both orientations of the  $B_y$  component in the solar wind. Color depicts the value of the  $B_x$  component. For ideal draping the  $B_x$  component in the +Y-MSO hemisphere must be negative for  $B_{y_{sw}} > 0$  (upper row). However, an unforeseen reversal of sign in  $B_x$  occurs near the terminator in the northern hemisphere

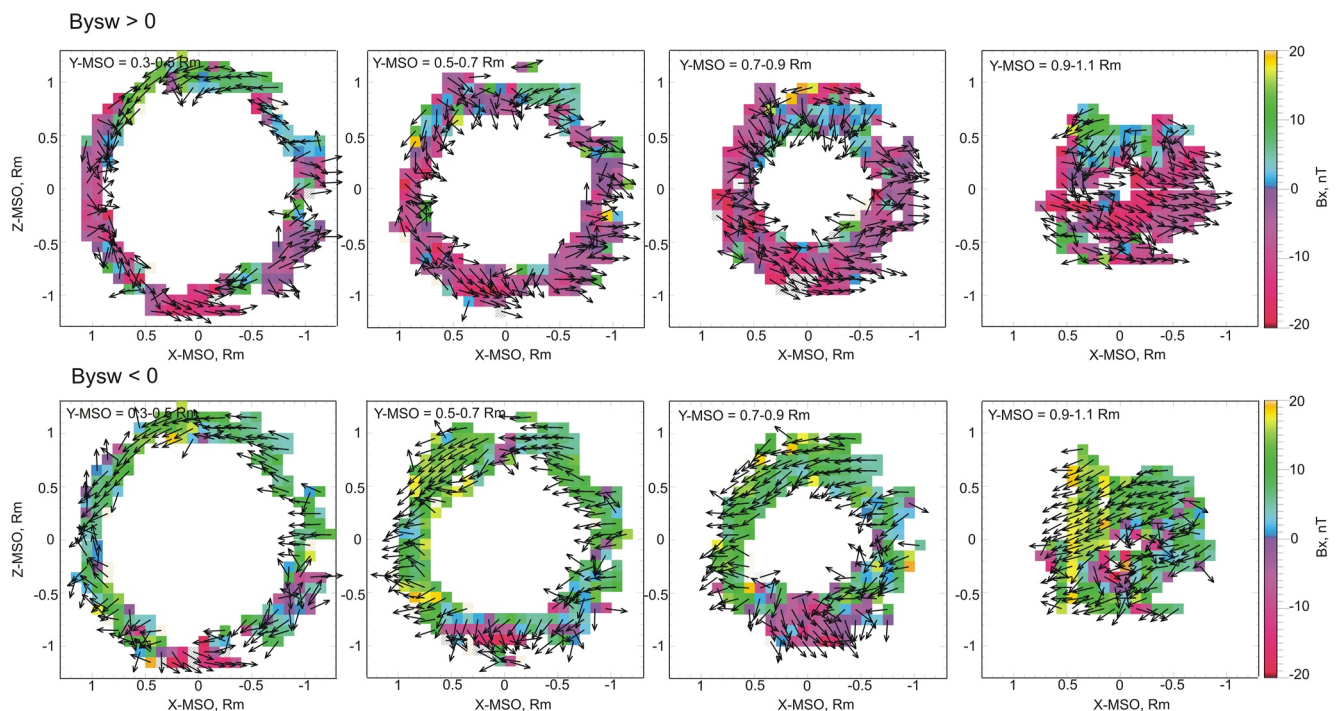


**Figure 5.** Projections of the unit vectors of the magnetic field onto the XZ-Mars Solar Orbital (MSO) planes for different ranges of Y-MSO for  $B_{y_{sw}} > 0$  and for  $B_{y_{sw}} < 0$ . Color shows the  $B_x$  component.

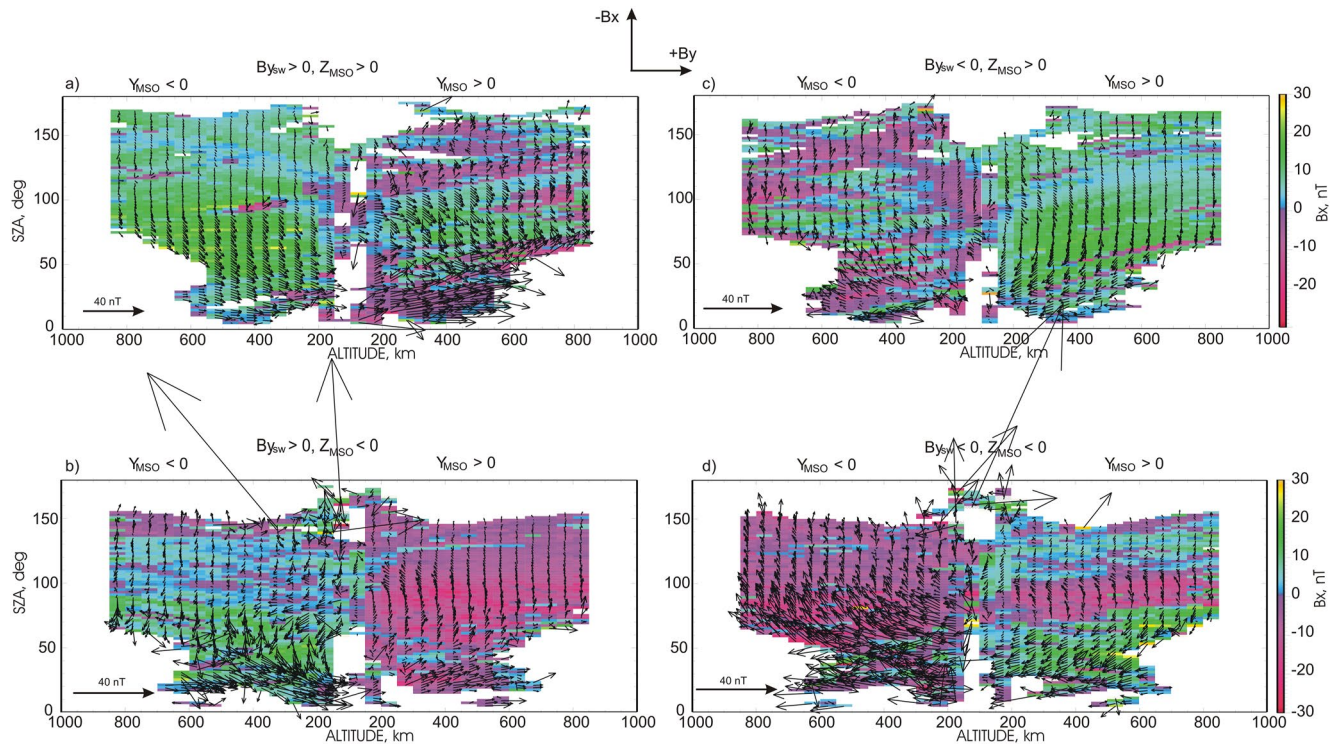


**Figure 6.** Projections of the magnetic field vector onto the Mars Solar Orbital XY plane ( $B_{xy}$ ) as a function of altitude and Solar Zenith Angle (SZA) in the northern and southern hemispheres for both orientations of the  $B_{y_{sw}}$ -component. Color shows the value of  $B_x$ .

( $B_x$  becomes positive). The size of this area increases with  $|Z|$ . For  $B_{y_{sw}} < 0$  (low row), the  $B_x$  component in the  $+Y$ -MSO hemisphere must be positive but now an unexpected reversal in  $B_x$  occurs in the southern hemisphere.

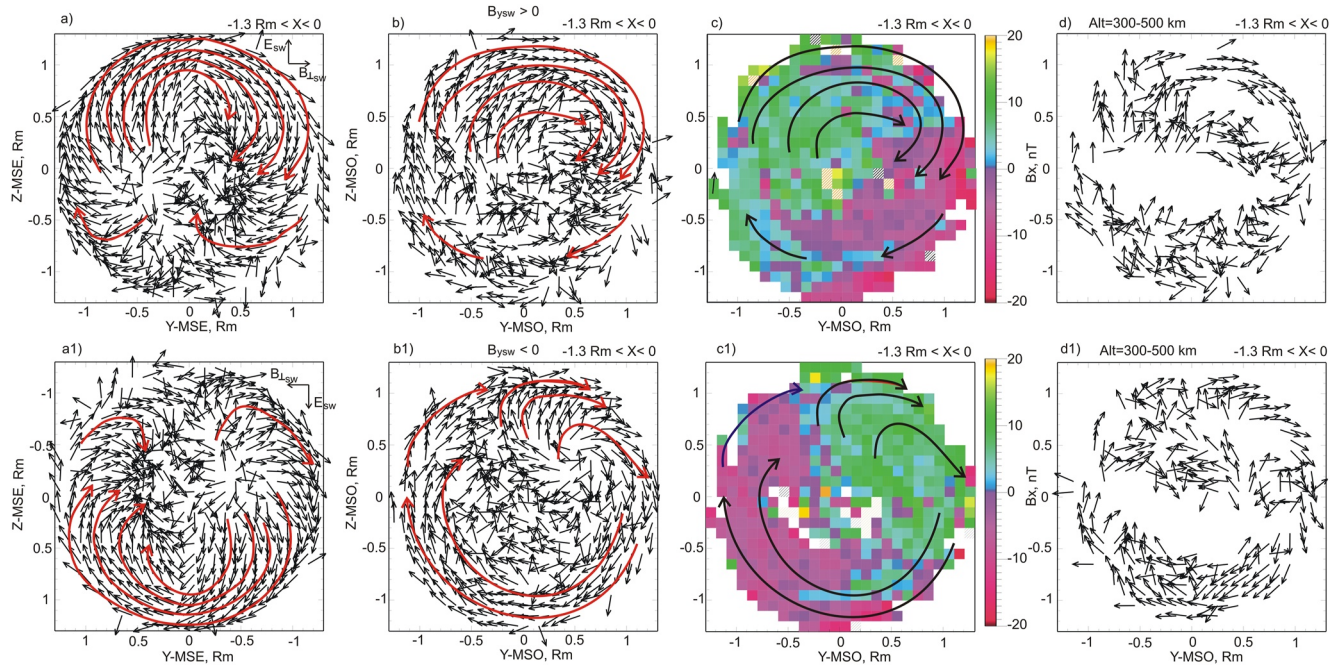
The reversal of the  $B_x$  component which is unusual for a draping topology occurs at all altitudes sampled by MAVEN. This is seen when plotting the projection of the magnetic field vector onto the MSO XY-plane ( $B_{xy}$ ) as a function of altitude and Solar Zenith Angle (SZA) in the northern and southern hemispheres for both orientations of the  $B_{y_{sw}}$  component (Figure 6). Color shows the value of  $B_x$ . In the northern hemisphere and for  $B_{y_{sw}} > 0$  (panel (a)), a broad band with unexpected reversal of sign of the  $B_x$  component occurs in the  $+Y$  hemisphere at  $60^\circ \leq \text{SZA} \leq 110^\circ$ . In contrast, in the  $-Y$  hemisphere we observe a classical draping geometry. With change of sign in  $B_{y_{sw}}$  a similar band appears in the  $-Y$  hemisphere while the features of classical draping are now seen in the  $+Y$  hemisphere (panel (c)). Correspondingly, at  $B_{y_{sw}} < 0$  a band with a reversal of the  $B_x$  component at  $Y > 0$  appears in the  $-Z$  hemisphere (panel (d)). Note also clear wrapping features (change of sign in the  $B_y$  component) in the  $-Z$ -hemisphere for  $B_{y_{sw}} > 0$  and in the  $+Z$ -hemisphere for  $B_{y_{sw}} < 0$ , both corresponding to the  $E^-$  hemisphere for the induced magnetosphere (Dubinin et al., 2018).

Figure 7 (panels (b) and (b1)) shows maps of the unit vectors of the magnetic field in the YZ-MSO planes at the nightside ( $X < 0$ ) and altitudes below 1,000 km for  $B_{y_{sw}} > 0$  and  $B_{y_{sw}} < 0$ , respectively. The data are presented in the same format as in Figure 4. In the MSE-coordinates (panels (a) and (a1)) we observe a distinct draping along the Z-axis in the so called  $E^+$  hemisphere in which the solar wind motional electric field is directed outward the ecliptic plane. In the opposite hemisphere a picture is more perturbed with a reversal of the  $B_y$ -component due to a wrapping of the field lines. In the MSO-coordinates we observe similar features but with a distinct twisting of the magnetic field in accordance with the sign of the  $B_{y_{sw}}$  component.

#### 4. Discussion

The flow pattern of oxygen ions in the outer part of the Martian magnetosphere is controlled by the sign of the  $B_{y_{sw}}$  component with a vertical flipping of the ion plume. A clear north—south asymmetry of the magnetosphere shaping seen at  $B_{y_{sw}} > 0$  is caused by the joint effect of the extension of the magnetosheath asymmetry toward the





**Figure 7.** Same as for Figure 4 but for the nightside ( $-1.3R_M < X < 0$ ).

tail due to multi-fluid interaction (Dubinin et al., 2018; Romanelli et al., 2020) and an enlargement of the magnetospheric obstacle due to the crustal magnetic field (Brain et al., 2005; Crider et al., 2002; Dubinin et al., 2008). At  $B_{ysw} < 0$ , when these effects occur in the opposite hemispheres, the shape of the magnetosphere becomes more symmetric.

The ion trail of a dense and slowly moving plasma in the tail is shifted to the southern (northern) hemisphere for  $B_{ysw} > 0$  ( $B_{ysw} < 0$ ), respectively, implying a recoil effect related to ion ejection in the opposite hemisphere. Conventional single MHD models can not explain this effect. Note that a recent multi-fluid MHD model (Ma et al., 2019) shows a similar effect of a shift. A similar effect was also observed in experiments with an artificial comet (Valenzuela et al., 1986). Different mechanisms were put forward to explain such a shift. Chapman and Dunlop (1986) suggested that a shift of the magnetic field pile-up in the direction of the motional electric field produces a force  $-\nabla B^2$  in the opposite direction which shifts the plasma cloud. This is supported by the multi-fluid MHD model results Ma et al., 2019, (see Figures 2b and 2d, when strong crustal field is in the nightside (case 2) or turn off (case 3)). Papadopoulos and Lui (1986) assumed a cross-field drift of plasma with force acting in the downstream direction. Harold and Hassam (1994) suggested mechanisms related to Hall currents and multi-ion coupling. At Mars the situation is more complicated because after the BS the plasma flow is diverged. Presently, it is not clear which of the above mentioned recoil mechanisms is more important. A shift of the ion trail and the additional magnetic field draping along the Z axis also controlled by the  $B_y$  component in the solar wind are intimately related. However, their cause-effect relationships remain unclear.

An interesting feature is that the ion trail is generally observed in the region where the  $B_y$  component changes sign. Wrapping of the magnetic field lines around Mars with a change of sign of  $B_y$  can be favorable for their further reconnection. A signature of reconnection might be the appearance of sunward plasma flows. Figure 8 (panels a and a1) show in the XZ-MSO planes maps of the unit vectors of the velocity of oxygen ions ( $O^+$  and  $O_2^+$ ) for cases with  $V_x > 0$  and different signs of  $B_{ysw}$ . Cases with the sunward component of the velocity in the tail were predominantly observed in the regions of the dense ion trail and are therefore sensitive to the sign of  $B_{ysw}$ . This is more clearly seen for intervals with  $B_{ysw} < 0$ . There is also a certain correlation with the sign of the local  $B_y$  component of the magnetic field (panels (b) and (b1)). It is worth noting that sunward fluxes are also observed without a change of sign of the  $B_y$  component. Panels (c) and (c1) present statistics (number of cases) of the observations with sunward fluxes ( $V_x > 0$ ). We see that the number of events in the southern hemisphere at

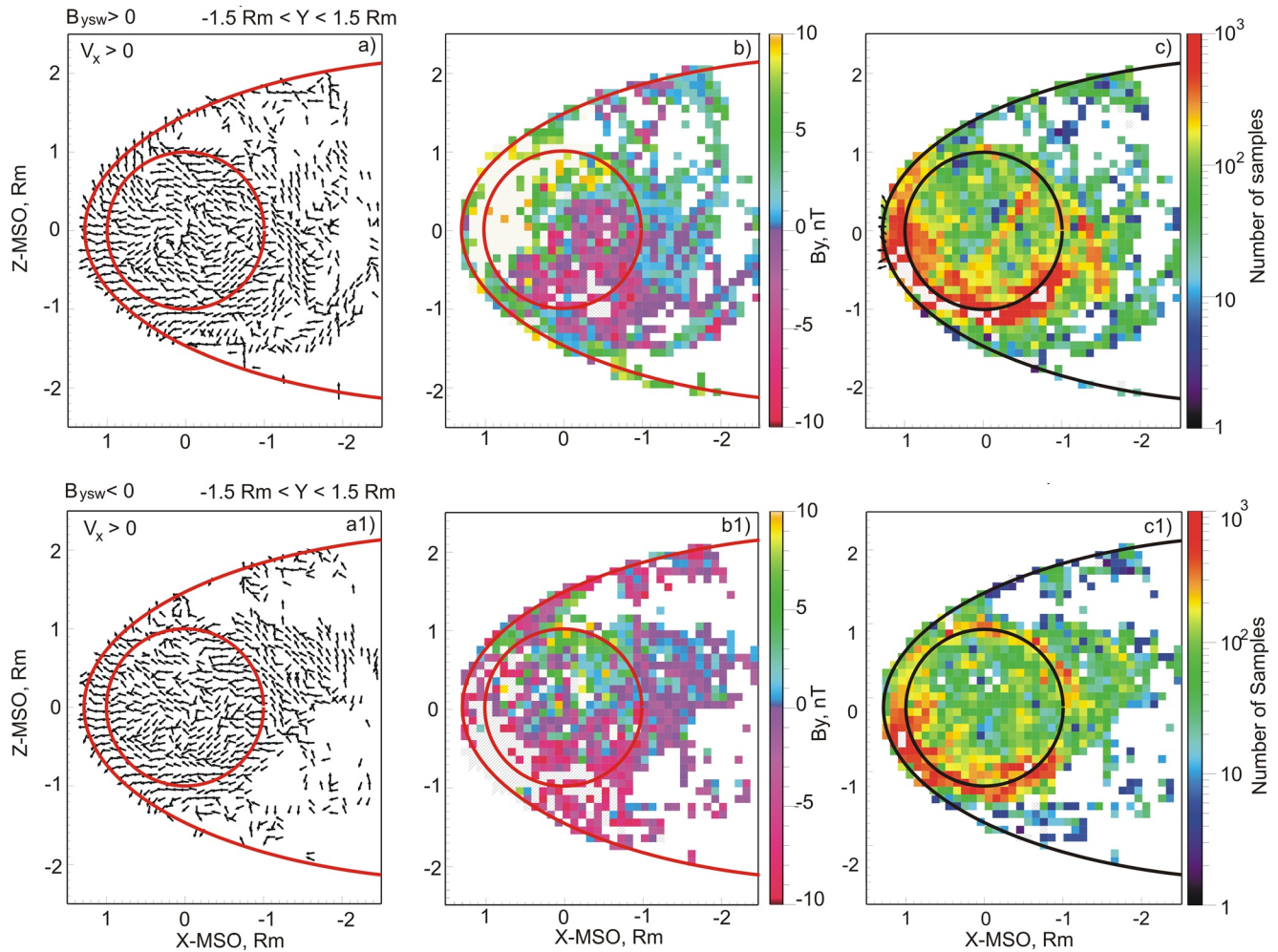


**Figure 8.** (a) and (a1): Maps of the unit vectors of the velocity of oxygen ions ( $O^+$  and  $O_2^+$ ) for cases with  $V_x > 0$  and different signs of  $B_{y_{sw}}$ ; (b) and (b1):  $B_y$  component of the magnetic field; (c) and (c1): number of the observations with  $V_x > 0$ . Statistically mean position of the magnetospheric boundary (Dubinin et al., 2006; Vignes et al., 2000) is also shown.

lower altitudes with crustal field sources is more than one order magnitude higher than the number of cases in the ion trail implying that reconnection processes are mostly related with the existence of the crustal magnetic fields.

The observed global twisting of the magnetic tail found earlier (DiBraccio et al., 2018, 2022; Dubinin et al., 2017) already arises at the dayside and propagates downstream. The topology of the crustal magnetic field is so complex that an obvious question is—why do we observe a statistically steady twisting of the field lines in the direction which is determined by the sign of the  $B_{y_{sw}}$  component in the solar wind. A similar twisting was observed in laboratory simulation experiments (Dubinin et al., 1980) in which a weak magnetic dipole was immersed into the obstacle with an artificial ionospheric shell. A twisting occurred due to the reconnection of the magnetic field embedded into the plasma flow and the dipole field. With the reversal of the dipole orientation a twisting occurred in the opposite direction. Although the crustal field on Mars is much more intricate than the dipole magnetic field one may expect that due to the used averaging over many planetary rotations a contribution of the high-order harmonics is strongly attenuated and the low-order harmonics of the crustal magnetic field dominate.

Figure 9 (panel (a)) shows a map of the median values of the  $B_x$  component of the crustal magnetic field on Mars in the  $YZ$ -plane in the Cain' model (Cain et al., 2003) applied for all orbits sampled by MAVEN within the Martian magnetosphere. We observe two lobes typical for the magnetic tail of dipole-type magnetosphere. Panel (a1) depicts the median values of the  $B_x$  component measured by MAVEN and plotted in MSE coordinates that reproduces the induced draping configuration. It is worth noting that although the model dipole component is in



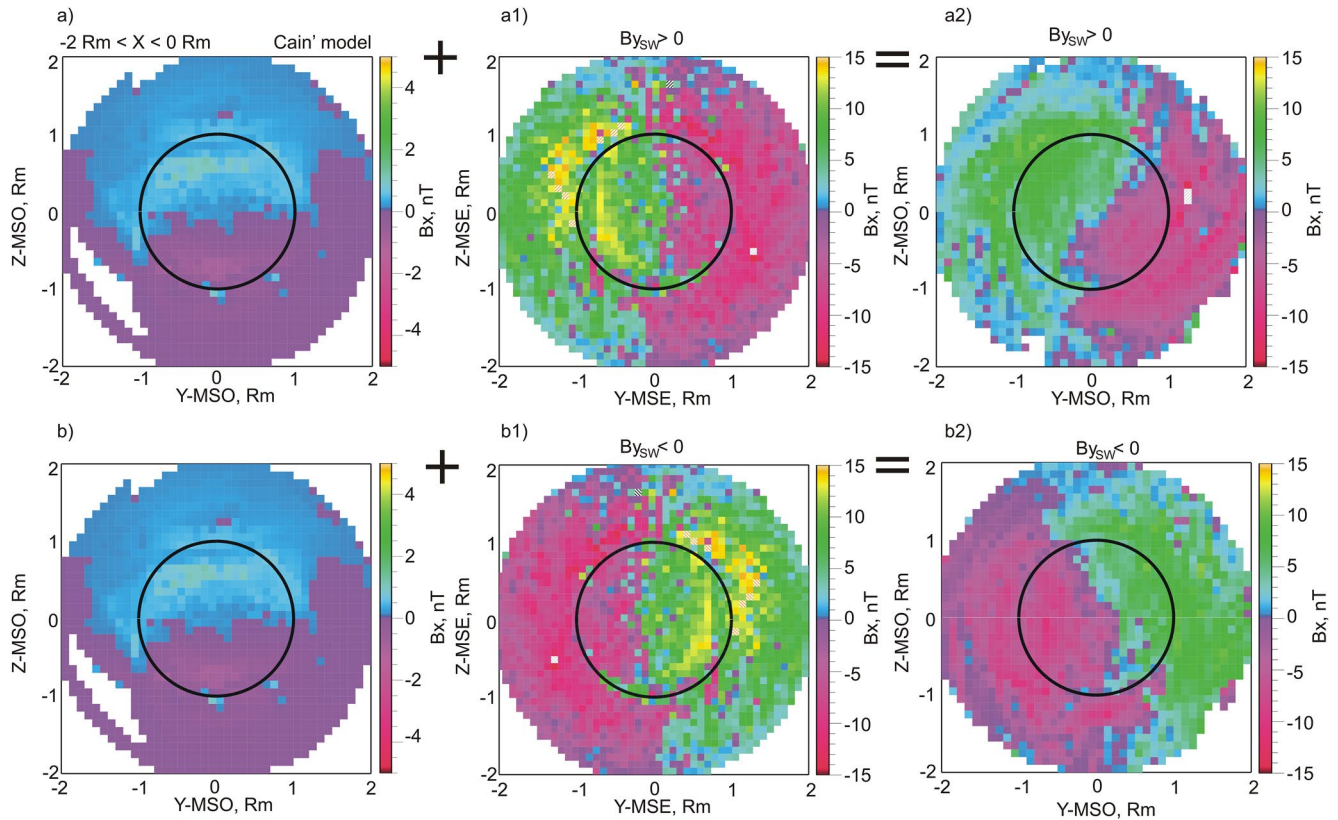


**Figure 9.** (a) Map of the median values of the  $B_x$  component of the crustal magnetic field on Mars in the YZ-plane in the Cain' model (Cain et al., 2003); (a1) map of the median values of the measured  $B_x$  component plotted in Mars Solar Electric coordinates; (a2) map of the  $B_x$  component in MSO coordinates for  $B_{y_{sw}} > 0$ ; panels (b)–(b2) show similar plots for  $B_{y_{sw}} < 0$ .

several times less than the observed value a stretching of the crustal field in the tail can significantly increase its value similar as it happens in the geomagnetic tail.

Panel (a2) presents a similar map obtained for all cases with  $B_{y_{sw}} > 0$  and characterized by a clockwise twisting of the magnetic field. It is seen that this map is a result of a 'superposition' of the classical draping pattern (panel (a1)) and a "dipole" component produced by a lower-order harmonics of the crustal field (panel (a)). Panel (b) is a replica of panel (a). Panel (b1) is a horizontally flipped panel (a1) corresponding to the draping configuration with a change of sign of the cross-flow component of the IMF in the solar wind. Panel (b2) shows a map obtained for the case of  $B_{y_{sw}} < 0$ . A twisting observed in the anticlockwise direction is a hybrid product of two types of magnetospheres.

Figure 10 shows how the model crustal field (Cain et al., 2003) looks like after averaging over many planetary rotations. Panel (a) depicts the unit vectors of the magnetic field projected onto the XZ-MSO plane. The data are presented only within the nominal boundary of the Martian magnetosphere. Color gives the value of the magnetic field. We see a dipole-like configuration and therefore it is not very surprising that we finally come to the twisted hybrid magnetosphere of Mars that is similar to the laboratory model (Dubinin et al., 1980). Panels (b) and (c) present maps of the unit vectors in the XY-MSO planes for  $Z > 0$  and  $Z < 0$  respectively. It is seen that for  $B_{y_{sw}} > 0$  we can expect that reconnection would occur in the  $+Y$  sector near the terminator in the northern hemisphere and in the  $-Y$  sector in the southern hemisphere. This is in agreement with our assumptions made from Figures 5 and 6. For  $B_{y_{sw}} < 0$  two other sectors are favorable for reconnection. Another important point is that because of the additional induced draping of the IMF along the Z-axis and the appearance of a strong  $B_z$  component, clearly seen for example, in Figure 4 (a,a1), a favorable area for reconnection must be in  $+Y$ -MSO sector in which  $B_z$  (induced)  $< 0$  and  $B_z$  (crustal)  $> 0$ . This is in agreement with the existence of stable bands with a reversed  $B_x$  component seen in panels of Figure 6. It is also in agreement with the conclusion by DiBraccio et al. (2022) that the reconnection likely occurs when a large shear is present between the IMF and crustal fields and most of the

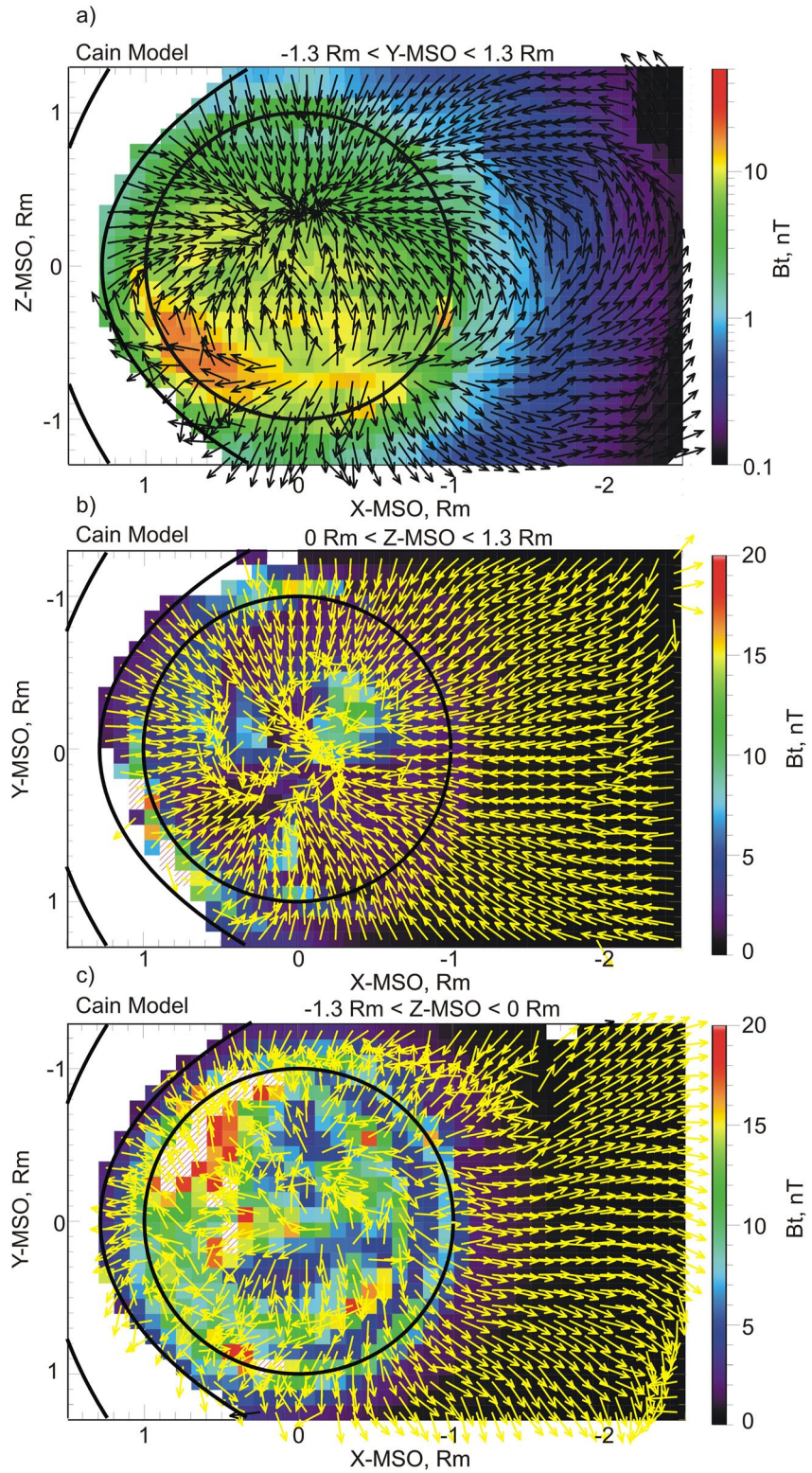


**Figure 10.** (a) The unit vectors of the model crustal field (Cain et al., 2003) projected onto the XZ-Mars Solar Orbital plane after averaging over many planetary rotations. Color shows the magnetic field value. (b and c) maps of the unit vectors of the model crustal field in the XY-MSO planes for the northern and southern hemispheres, respectively.



time twisting is larger for  $B_{y_{sw}} > 0$ . It is not clear yet whether a shift of the flow of oxygen ions toward the duskside (see Figures 2e and 2e1) is related to this enhanced reconnection in the +Y sector.

Figure 11 presents sketches of several segments of open field lines which have one end on the Mars surface and arise due to reconnection with a dipole component of the crustal magnetic field. Panel (a) and (b) show

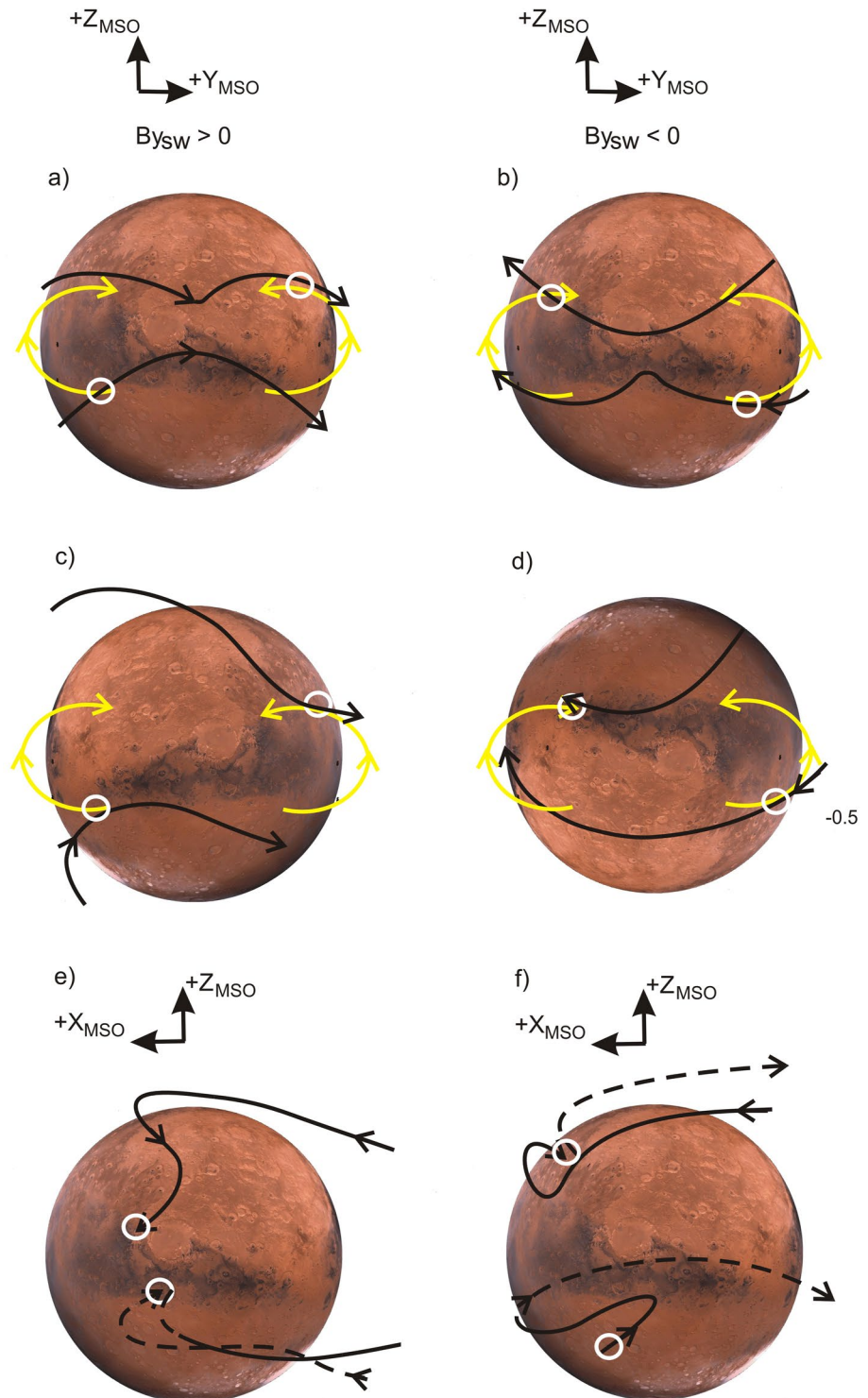


**Figure 11.** Sketches of several open field lines (black curves) due to reconnection with a dipole component of the crustal magnetic field (yellow curves).

projections onto the YZ-MSO plane of draping field lines (black curves) and crustal field lines (yellow curves) at the dayside before reconnection for  $B_{y_{sw}} > 0$  and  $B_{y_{sw}} < 0$ , respectively. The draping component is taken from Figures 4a and 4a1. White circles show expected sites for reconnection. Panels (c) and (d) depict the picture after reconnection with a skewness arising due to the asymmetrical motion of the magnetic flux tubes in the hemispheres with and without reconnection. Panels (e) and (f) present a possible geometry of the open field lines in the XZ-MSO plane based on the observations (view from the +Y direction). Such a picture can explain a statistically steady twisting of the whole magnetosphere of Mars.

It is interesting to note that Luhmann et al. (2015) have used a global MHD model of the solar wind/Mars interaction trying to reveal the influence of the lower-order moments of the crustal field (dipole component) on deviations from ideal draping observed by MGS at 400 km (Brain et al., 2006). The authors concluded that such an effect might be compromised by the contribution of the induced component. Analysis made in our paper shows that at least statistically, the effect of the low-order harmonics can lead to a rather coherent picture of reconnection and subsequently to a global hybrid magnetosphere of Mars. On the other hand, probably only simulations made for a preset IMF orientation and for a fixed crustal field geometry can clear up the significance of the low-order moments.

### Data Availability Statement

The MAVEN project is supported by NASA through the Mars Exploration Program. MAVEN data are publicly available through the Planetary Data System (<https://pds-ppi.igpp.ucla.edu/mission/MAVEN>).

### Acknowledgments

Authors ED, MP, ST wish to acknowledge support from DFG for supporting this work by Grants TE 664/4-1 and PA 525/25-1. Open Access funding enabled and organized by Projekt DEAL.

### References

- Acuña, M. H., Connerney, J. E. P., Ness, N. F., Lin, R. O., Mitchell, D., Carlson, C. W., et al. (1999). Global distribution of crustal magnetism discovered by Mars Global Surveyor MAG/ER experiment. *Science*, *284*(5415), 790–793. <https://doi.org/10.1126/science.284.5415.790>
- Andrews, D. J., Oppenoorth, H. J., Edberg, N. J. T., Andre, M., Fränz, M., Dubinin, E., et al. (2013). Determination of local plasma densities with the MARSIS radar: Asymmetries in the high altitude Martian ionosphere. *Journal of Geophysical Research: Space Physics*, *118*(10), 6228–6242. <https://doi.org/10.1002/jgra.50593>
- Brain, D., Halekas, J., Lillis, R., Mitchell, D., Lin, R., & Crider, D. (2005). Variability of the altitude of the Martian sheath. *Geophysical Research Letters*, *32*(1), 18203. <https://doi.org/10.1029/2005GL023126>
- Brain, D. A., Mitchel, D. L., & Halekas, J. S. (2006). The magnetic field draping direction at Mars from April 1999 through August 2004. *Icarus*, *182*(2), 465–473. <https://doi.org/10.1016/j.icarus.2005.09.023>
- Cain, J. C., Ferguson, B. B., & Mozzoni, D. (2003). An  $n = 90$  internal potential function of the Martian crustal magnetic field. *Geophysical Research Letters*, *108*, 5008. <https://doi.org/10.1029/2000JE001487>
- Chai, L., Wan, W., Wei, Y., Zhang, T., Exner, W., Fraenz, M., et al. (2019). The induced global looping magnetic field on Mars. *The Astrophysical Journal Letters*, *871*(2), L27. <https://doi.org/10.3847/2041-8213/aaff6e>
- Chapman, S., & Dunlop, M. (1986). Ordering of momentum transfer along one dimension in the AMPTE solar wind release. *Journal of Geophysical Research*, *91*(A7), 8051. <https://doi.org/10.1029/ja091ia07p08051>
- Connerney, J. E. P., Acuna, M. H., Ness, N. F., Kletetschka, G., Mitchell, D. L., Lin, R. P., & Reme, H. (2005). Tectonic implications of Mars crustal magnetism. *Proceedings of the National Academy of the Sciences of the United States of America*, *102*(42), 14970–14975. <https://doi.org/10.1073/pnas.0507469102>
- Connerney, J. E. P., Espley, J., Lawton, P., Murphy, S., Odom, J., Olivers, R., & Sheppard, D. (2015). The MAVEN magnetic field investigation. *Space Science Reviews*, *195*(1–4), 257–291. <https://doi.org/10.1007/s11214015-0169-4>
- Crider, D. H., Acuna, M. H., Connerney, J. E. P., Vignes, D., Ness, N. F., Krymskii, A. M., et al. (2002). Observations of latitude dependence of the location of the Martian pileup boundary. *Geophysical Research Letters*, *29*(8), 1170–1211-4. <https://doi.org/10.1029/2001GL013860>
- DiBraccio, G., Romanelli, N., Bowers, C., Gruesbeck, J., Halekas, J., Ruhunisir, S., et al. (2022). A statistical investigation of factors influencing the magnetotail twist at Mars. *Geophysical Research Letters*, *49*(12), e2022GL098007. <https://doi.org/10.1029/2021GL096764>
- DiBraccio, G. A., Luhmann, J. G., Curry, S. M., Espley, J. R., Xu, S., Mitchell, D. L., et al. (2018). The twisted configuration of the Martian magnetotail: MAVEN observations. *Geophysical Research Letters*, *45*(10), 4559–4568. <https://doi.org/10.1029/2018GL077251>
- Dong, Y., Fang, X., Brain, D. A., Hurley, D. M., Halekas, J. S., Espley, J. R., et al. (2019). Magnetic field in the Martian magnetosheath and the application as an IMF clock angle proxy. *Journal of Geophysical Research: Space Physics*, *124*(6), 4295–4313. <https://doi.org/10.1029/2019JA026522>
- Dong, Y., Fang, X., Brain, D. A., McFadden, J. P., Halekas, J. S., Connerney, J. E., et al. (2015). Strong plume fluxes at Mars observed by MAVEN: An important planetary ion escape channel. *Geophysical Research Letters*, *42*(21), 8942–8950. <https://doi.org/10.1002/2015GL065346>
- Dubinin, E., Chanteur, G., Fraenz, M., Modolo, R., Woch, J., Roussos, E., et al. (2008). Asymmetry of plasma fluxes at Mars: ASPERA-3 observations and hybrid simulations. *Planetary and Space Science*, *56*(6), 832–835. <https://doi.org/10.1016/j.pss.2007.12.006169>
- Dubinin, E., Fraenz, M., Andrews, D., & Morgan, D. (2016). Martian ionosphere observed by Mars Express, 1. Influence of the crustal magnetic fields. *Planetary and Space Science*, *124*, 62–75. <https://doi.org/10.1016/j.pss.2016.02.004>
- Dubinin, E., Fraenz, M., Fedorov, A., Lundin, R., Edberg, N., Duru, F., & Vaisberg, O. (2011). Ion energization and escape on Mars and Venus. *Space Science Reviews*, *162*(1–4), 173–211. <https://doi.org/10.1007/978-1-4614-3290-6-6>
- Dubinin, E., Fraenz, M., Modolo, R., Pätzold, M., Tellmann, S., Vaisberg, O., et al. (2021). Induced magnetic fields and plasma motions in the inner part of the Martian magnetosphere. *Journal of Geophysical Research: Space Physics*, *126*(12), e2021JA029542. <https://doi.org/10.1029/2021JA029542>



- Dubinin, E., Fraenz, M., Pätzold, M., McFadden, J., Halekas, J. S., DiBraccio, G. A., et al. (2017). The effect of solar wind variations on the escape of oxygen ions from Mars through different channels: MAVEN observations. *Journal of Geophysical Research: Space Physics*, *122*(11), 11285–11301. <https://doi.org/10.1002/2017JA024741>
- Dubinin, E., Fraenz, M., Pätzold, M., Woch, J., McFadden, J., Fan, K., et al. (2020). Impact of Martian crustal magnetic field on the ion escape. *Journal of Geophysical Research: Space Physics*, *125*(10), e2020JA028010. <https://doi.org/10.1029/2020JA028010>
- Dubinin, E., Fraenz, M., Woch, J., Modolo, R., Chanteur, G., Duru, F., et al. (2012). Upper ionosphere of Mars is not axially symmetrical, Earth. *Planets and Space*, *64*(113), 113–120. <https://doi.org/10.5047/eps.2011.05.022>
- Dubinin, E., Fraenz, M., Woch, J., Roussos, E., Barabash, S., Lundin, R., et al. (2006). Plasma morphology at Mars: ASPERA-3 observations. *Space Science Reviews*, *126*(1–4), 209–238. <https://doi.org/10.1007/s11214-006-9039-4>
- Dubinin, E., Israelevich, P. L., & Podgomy, I. M. (1980). Combined magnetosphere. *Cosmic Research English Translation*, *18*, 470.
- Dubinin, E., Luhmann, J., & Slavin, J. (2020). Solar wind and terrestrial planets. In *Oxford research encyclopedia of planetary science*. Oxford University Press. <https://doi.org/10.1093/acrefore/9780190647926.013.184>
- Dubinin, E., Modolo, R., Fraenz, M., Pätzold, M., Woch, J., Chai, L., et al. (2018). The induced magnetosphere of Mars: Asymmetrical topology of the magnetic field lines. *Geophysical Research Letters*, *46*(22), 12722–12730. <https://doi.org/10.1029/2019GL084387>
- Dubinin, E., Sauer, K., Lundin, R., Norberg, O., Trotignon, J.-G., Schwingenschuh, K., et al. (1996). Plasma characteristics of the boundary layer in the Martian magnetosphere. *Journal of Geophysical Research*, *101*(A12), 27061–27075. <https://doi.org/10.1029/96ja02021>
- Fan, K., Fraenz, M., Wei, Y., Cui, J., Rong, Z., Chai, L., & Dubinin, E. (2020). Deflection of global ion flow by the Martian crustal magnetic fields. *The Astrophysical Journal Letters*, *898*(2), L54. <https://doi.org/10.3847/2041-8213/aba519>
- Fan, K., Fraenz, M., Wei, Y., Han, Q., Dubinin, E., Cui, J., et al. (2019). Reduced atmospheric ion escape above Martian crustal magnetic fields. *Geophysical Research Letters*, *46*(21), 11764–11772. <https://doi.org/10.1029/2019GL084729>
- Fang, X., Ma, Y., Brain, D., Dong, Y., & Lillis, R. (2015). Control of Mars global atmospheric loss by the continuous rotation of the crustal magnetic field: A time-dependent MHD study. *Journal of Geophysical Research: Space Physics*, *120*(12), 10926–10944. <https://doi.org/10.1002/2015JA021605>
- Fang, X., Ma, Y., Masunaga, K., Dong, Y., Brain, D., Halekas, J., et al. (2017). The Mars crustal magnetic field control of plasma boundary locations and atmospheric loss: MHD prediction and comparison with MAVEN. *Journal of Geophysical Research: Space Physics*, *122*(4), 4117–4137. <https://doi.org/10.1002/2016JA023509>
- Garnier, P., Jacquey, C., Gendre, X., Génot, V., Mazelle, C., Fang, X., et al. (2022). The drivers of the Martian bow shock location: A statistical analysis of Mars atmosphere and volatile Evolution and Mars express observations. *Journal of Geophysical Research: Space Physics*, *127*(5), e2021JA030147. <https://doi.org/10.1029/2021JA030147>
- Girazian, Z., Schneider, N. M., Milby, Z., Fang, X., Halekas, J., Weber, T., et al. (2021). Discrete aurora at Mars: Dependence on upstream solar wind conditions. *Journal of Geophysical Research: Space Physics*, *127*(4), e2021JA030238. <https://doi.org/10.1029/2021JA030238>
- Halekas, J., Luhmann, J. G., Dubinin, E., & Ma, Y. (2021). Induced magnetospheres: Mars. In B. Editor(s), R. Maggiolo, N. Andre, H. Hasegawa, D. Welling, Y. Zhang, et al. (Eds.), *In book magnetospheres in solar system, geophysics monograph series*. <https://doi.org/10.1002/9781119815624.ch25>
- Halekas, J. S., Brain, D. A., Luhmann, J. G., DiBraccio, G. A., Ruhunusiri, S., Harada, Y., et al. (2017). Flows, fields, and forces in the Mars-solar wind interaction. *Journal of Geophysical Research: Space Physics*, *122*(11), 11320–11341. <https://doi.org/10.1002/2017JA024772>
- Halekas, J., Taylor, E., Dalton, G., Johnson, G., Curtis, D., McFadden, J., et al. (2015). The solar wind ion analyzer for MAVEN. *Space Science Reviews*, *195*(1–4), 125–151. <https://doi.org/10.1007/s11214-013-0029-z>
- Harold, J. B., & Hassam, A. B. (1994). Two ion fluid numerical investigations of solar wind gas releases. *Journal of Geophysical Research*, *99*(A10), 19325–19340. <https://doi.org/10.1029/94ja00790>
- Jakosky, B. M., Lin, R. P., Grebowsky, J. M., Luhmann, J. G., Mitchell, D. F., Beutelschies, G., et al. (2015). The Mars atmosphere and volatile evolution (MAVEN) mission. *Space Science Reviews*, *195*(1–4), 3–48. <https://doi.org/10.1007/s11214-015-0139-x>
- Lavraud, B., & Larson, D. (2016). Correcting moments of in-situ particle distribution functions for spacecraft electrostatic charging. *Journal of Geophysical Research: Space Physics*, *121*(9), 8462–8474. <https://doi.org/10.1002/2016JA022591>
- Lillis, R., Mitchell, D., Steckleviez, M., Brain, D., Xu, S., Weber, T., et al. (2018). Ionizing electrons on the Martian nightside. Structure and variability. *Journal of Geophysical Research: Space Physics*, *123*(5), 4349–4363. <https://doi.org/10.1029/2017JA025151>
- Liu, D., Rong, Z., Gao, J., He, J., Klinger, L., Dunlop, M., et al. (2021). Statistical properties of solar wind upstream of Mars, MAVEN observations. *The Astrophysical Journal*, *911*(10), 113. <https://doi.org/10.3847/1538-4357/abed50>
- Luhmann, J. G., Ma, Y.-J., Brain, D., Ulusen, D., Lillis, R., Halekas, J., & Espley, J. (2015). Solar wind interaction effects on the magnetic field around Mars: Consequences for interplanetary and crustal field measurements. *Planetary and Space Science*, *117*, 15–23. <https://doi.org/10.1016/j.pss.2015.05.004>
- Ma, Y. J., Dong, C. F., Toth, G., Van der Holst, B., Nagy, A. F., Russell, C. T., et al. (2019). Importance of ambipolar electric field in driving ion loss from Mars: Results from a multifluid MHD model with the electron pressure equation included. *Journal of Geophysical Research: Space Physics*, *124*(11), 9040–9057. <https://doi.org/10.1029/2019JA027091>
- McFadden, J. P., Kortmann, O., Curtis, D., Dalton, G., Johnson, G., Abiad, R., et al. (2015). MAVEN SupraThermal and thermal ion composition (STATIC) instrument. *Space Science Reviews*, *195*(1–4), 199–256. <https://doi.org/10.1007/s11214-015-175-6>
- Moore, K. R., McComas, D. J., Russell, C. T., & Mihalov, J. D. (1990). A statistical study of ions and magnetic field in the Venus magnetotail. *Journal of Geophysical Research*, *95*(A8), 12005. <https://doi.org/10.1029/ja095ia08p12005>
- Nagy, A. F., Winterhalter, D., Sauer, K., Cravens, T., Brecht, S., Mazelle, C., et al. (2004). The plasma environment of Mars. *Space Science Reviews*, *111*(1/2), 238–114. <https://doi.org/10.1023/b:spac.0000032718.47512.92>
- Papadopoulos, K., & Lui, A. T. Y. (1986). On the initial motion of artificial comets in the AMPTE releases. *Geophysical Research Letters*, *13*(9), 925–927. <https://doi.org/10.1029/g1013i009p00925>
- Ramstad, R., Brain, D., Dong, Y., Espley, J., Halekas, J., & Jakosky, B. (2020). The global current systems of the Martian induced magnetosphere. *Nature Astronomy*, *4*(10), 979–985. <https://doi.org/10.1038/s41550-020-1099-y>
- Romanelli, N., DiBraccio, G., Halekas, J., Dubinin, E., Gruesbeck, J., Espley, J., et al. (2020). Variability of the solar wind flow asymmetry in the Martian magnetosheath observed by MAVEN. *Geophysical Research Letters*, *47*(22), e2020GL090793. <https://doi.org/10.1029/2020GL090793>
- Russell, C. T., Mulligan, T., Delva, M., Zhang, T.-L., & Schwingenschuh, K. (1995). A simple test of the induced nature of the Martian tail. *Planetary and Space Science*, *43*(7), 875–879. [https://doi.org/10.1016/0032-0633\(94\)00217-f](https://doi.org/10.1016/0032-0633(94)00217-f)
- Schneider, N., Milby, Z., Jain, S., Gerard, J.-C., Soret, L., Brain, D. A., et al. (2021). Discrete aurora on Mars: Insights into their distribution and activity from MAVEN/IUVS observations. *Journal of Geophysical Research: Space Physics*, *126*(10), e2021JA029428. <https://doi.org/10.1029/2021JA029428>

- Simon Wedlund, C., Volwerk, M., Beth, A., Mazelle, C., Möstl, C., Halekas, J., et al. (2022). A fast bow shock location predictor-estimator from 2D and 3D analytical models: Application to Mars and the MAVEN mission. *Journal of Geophysical Research: Space Physics*, 127(1), e2021JA029942. <https://doi.org/10.1029/2021JA029942>
- Valenzuela, A., Haerendel, G., Fopple, H., Melzner, F., Neuss, H., Rieger, E., et al. (1986). The AMPTE artificial comet experiments. *Nature*, 320(6064), 700–703. <https://doi.org/10.1038/320700a0>
- Vignes, D., Mazelle, C., Rme, H., Acuña, M. H., Connerney, J. E. P., Lin, R. P., et al. (2000). The solar wind interaction with Mars: Locations and shapes of the bow shock and the magnetic pile-up boundary from the observations of the MAG/ER Experiment onboard Mars Global Surveyor. *Geophysical Research Letters*, 27(1), 49–52. <https://doi.org/10.1029/1999GL010703>
- Weber, T., Brain, D., Mitchell, D., Xu, S., Connerney, J., & Halekas, J. (2017). Characterization of low-altitude nightside Martian magnetic topology using electron pitch angle distributions. *Journal of Geophysical Research: Space Physics*, 122(10), 9777–9789. <https://doi.org/10.1002/2017JA024491>
- Weber, T., Brain, D., Mitchell, D., Xu, S., Espley, J., Halekas, J., et al. (2019). Influence of solar wind pressure on Martian crustal magnetic field topology. *Geophysical Research Letters*, 46(5), 2347–2354. <https://doi.org/10.1029/2019GL081913>
- Weber, T., Brain, D., Xu, S., Mitchell, D., Espley, J., Halekas, J., et al. (2020). The influence of interplanetary magnetic field direction on Martian crustal magnetic field topology. *Geophysical Research Letters*, 47(19), e2020GL087757. <https://doi.org/10.1029/2020GL087757>
- Weber, T., Brain, D., Xu, S., Mitchell, D., Espley, J., Mazelle, C., et al. (2021). Martian crustal field influence on O+ and O2+ escape as measured by MAVENFirst published: 08 August 2021. *Journal of Geophysical Research: Space Physics*, 126(8), e2021JA029234. <https://doi.org/10.1029/2021JA029234>
- Xu, S., Mitchell, D., Liemohn, M., Fang, X., Ma, Y., Luhmann, J., et al. (2017). Martian low-altitude magnetic topology deduced from MAVEN/SWEA observations. *Journal of Geophysical Research: Space Physics*, 122(2), 1831–1852. <https://doi.org/10.1002/2016JA023467>
- Xu, S., Mitchell, D. L., Weber, T., Brain, D. A., Luhmann, J. G., Dong, C., et al. (2020). Characterizing Mars's magnetotail topology with respect to the upstream interplanetary magnetic fields. *Journal of Geophysical Research: Space Physics*, 125(3), e2019JA027755. <https://doi.org/10.1029/2019JA027755>
- Xu, S., Weber, T., Mitchell, D. L., Brain, D. A., Mazelle, C., DiBraccio, G. A., & Espley, J. (2019). A technique to infer magnetic topology at Mars and its application to the terminator region. *Journal of Geophysical Research: Space Physics*, 124(3), 1823–1842. <https://doi.org/10.1029/2018JA026366>
- Yeroshenko, Y., Riedler, W., Schwingenschuh, K., Luhmann, J. G., Ong, M., & Russell, C. T. (1990). Magnetotail of Mars: Phobos observations. *Geophysical Research Letters*, 17(6), 885–888. <https://doi.org/10.1029/g1017i006p00885>